processes

MDPI

Article

Numerical Investigation of Coal and Rice Husk Co-Combustion in an Industrial-Scale Circulating Fluidized Bed: Hydrodynamics, Temperature, and Pollutant Emissions

Li Liu [1,2], Jiahe Sun [3], Ye Shui Zhang [4], Tanzila Anjum [3], Dongkuan Zhang [3], Junchao Yang [3], Jingliang Dong [4], Shaokoon Cheng [5] and Guozhao Ji [3,*]

1 Key Laboratory of Hubei Province for Coal Conversion and New Carbon Materials, Wuhan University of Science and Technology, Wuhan 430081, China
2 Anhui Conch Biomass Energy Technol Co., Ltd., Wuhu 241000, China
3 Key Laboratory of Industrial Ecology and Environmental Engineering of Ministry of Education, School of Environmental Science and Technology, Dalian University of Technology, Dalian 116000, China
4 Institute for Sustainable Industries & Liveable Cities, Victoria University, P.O. Box 14428, Melbourne, VIC 3011, Australia
5 School of Engineering, Macquarie University, Sydney, NSW 2109, Australia
* Correspondence: guozhaoji@dlut.edu.cn

Abstract

Co-firing biomass with coal in existing circulating fluidized bed (CFB) boilers is a promising strategy for reducing net CO_2 emissions and utilizing renewable energy. However, the impact of biomass-blending ratio on the complexity of multiphase flow, combustion characteristics, and pollutant formation inside a full-scale CFB boiler is not fully understood yet. This study developed Eulerian–Lagrangian Multiphase Particle-In-Cell (MP-PIC) model and this model was employed to simulate the co-combustion of coal and rice husk in a 72 MW industrial-scale CFB boiler. The pyrolysis kinetics of the coal and biomass were first measured experimentally via thermogravimetric analyzer and integrated into the model via source terms. The experimentally validated model was further used to investigate the effects of biomass-blending ratio (0–40 wt.%) on hydrodynamics, temperature distribution, and gaseous pollutant emissions (NO, SO_2). Results indicated that biomass addition has a negligible impact on the overall particle flow patterns and particle volume fraction distribution in the boiler. However, it significantly lowered the average furnace temperature due to the lower calorific value of biomass. A blending ratio of 40 wt.% biomass yielded the most substantial reduction in pollutant emissions at the outlet, with decreases of 51.99% for CO_2, 15.70% for NO, and 49.50% for SO_2 compared to single coal combustion. This study presents the MP-PIC model as an efficient numerical framework for optimizing co-firing operations and shows that a high ratio of biomass co-firing (40 wt.%) is technically feasible and environmentally advantageous in existing CFB boilers.

Keywords: circulating fluidized bed (CFB); co-combustion; MP-PIC; Numerical Simulation; biomass; pollutant emissions; pyrolysis kinetics

Check for updates

Academic Editor: Fabrizio Scala

Received: 14 May 2026
Revised: 1 July 2026
Accepted: 2 July 2026
Published: 4 July 2026

Copyright: © 2026 by the authors. Licensee MDPI, Basel, Switzerland. This article is an open access article distributed under the terms and conditions of the Creative Commons Attribution (CC BY) license.

1. Introduction

The global energy sector is undergoing a serious transformation, facing enormous stress to decarbonize and reduce the historical reliance on coal, a primary source of anthropogenic CO_2 emissions and harmful gaseous pollutants. Strategies for an environmentally

friendly and sustainable energy transition are urgently desired. Biomass, as a carbon-neutral (or even negative) fuel, has emerged as a promising alternative to coal due to the reduced net CO_2 emissions when combusted. However, its large-scale application in power generation faces many constraints. Importantly, coal historically has been a leading energy source globally, especially in regions with abundant coal reserves (Table 1). Complete phase-out is infeasible in the short-to-medium term due to energy supply concerns, existing infrastructure investments, and the need to meet growing electricity demand. Co-firing carbon-neutral biomass together with coal in existing power plants represents a practical and transitional pathway to lower the carbon footprint of power generation and mitigate emissions. This strategy could also avoid the high cost and time of a complete infrastructure refurbishment [1,2]. Among combustion technologies, circulating fluidized bed (CFB) boilers are particularly appropriate for the co-firing strategy due to CFB's inherent fuel flexibility [3]. The successful implementation of co-firing requires a deep understanding of the complex differences and interactions between coal and biomass within the boiler system, which remains a key technical challenge [4–6].

Table 1. Electricity generation from different types of fuels in different countries and regions (2023) [7].

Country or Region	Coal	Oil	Natural Gas	Nuclear Energy	Hydropower	Renewable Energy	Others	Total
Canada	34.1	2.7	81.0	86.6	398.4	52.1	4.7	659.6
Mexico	21.9	34.2	191.8	10.8	35.7	46.2	-	340.7
United States	904.2	25.1	1816.6	812.1	258.6	719.5	11.5	4547.7
Argentina	2.1	16.7	80.4	7.5	23.9	19.4	0.8	150.8
Brazil	16.5	10.1	42.1	14.6	427.1	164.5	2.3	677.2
France	3.1	2.3	46.9	294.7	44.6	68.0	8.1	467.7
Germany	180.6	4.4	79.8	34.7	17.5	236.5	23.8	577.3
Italy	17.6	9.7	156.3	-	28.2	72.0	3.6	287.3
Netherlands	17.3	1.6	47.8	4.2	0.1	48.3	2.7	122.0
Poland	127.4	1.7	11.6	-	2.0	34.7	1.7	179.1
Spain	9.4	10.1	89.3	58.6	18.2	103.3	4.9	293.7
Turkey	112.8	3.1	71.8	-	67.2	71.4	-	326.2
Ukraine	24.8	0.5	7.2	62.1	11.1	7.0	-	112.7
United Kingdom	5.6	2.1	125.3	47.7	5.3	129.5	10.5	326.0
Kazakhstan	76.8	0.1	23.7	-	9.2	4.2	-	114.0
Russia	192.3	6.7	533.9	223.7	197.7	7.4	5.3	1166.9
Iran	0.8	31.2	300.2	6.6	7.5	2.0	-	348.1
Saudi Arabia	-	131.4	269.4	-	-	0.8	-	401.6
United Arab Emirates	-	-	127.7	20.1	-	7.0	-	154.7
Egypt	-	17.6	159.3	-	13.8	10.2	-	200.8
South Africa	197.2	3.6	-	10.1	3.1	16.3	4.5	234.8
Australia	130.9	5.0	46.3	-	17.1	73.7	0.5	273.6
Mainland China	5397.8	11.9	290.6	417.8	1303.1	1367.0	60.4	8848.7

Table 1. *Cont.*

Country or Region	Coal	Oil	Natural Gas	Nuclear Energy	Hydropower	Renewable Energy	Others	Total
India	1380.1	2.5	47.0	46.2	174.9	205.9	1.3	1858.0
Indonesia	205.3	6.1	56.1	-	27.3	38.0	0.6	333.4
Japan	309	40.6	319.7	51.8	74.9	152.1	85.4	1033.6
Malaysia	76.4	1.8	68.4	-	32.5	3.9	-	182.9
South Korea	208.7	6.9	173.3	176.1	3.5	47.7	4.2	620.3
Thailand	35.5	1.7	114.6	-	6.6	21.9	-	180.4
Vietnam	100.8	0.7	27.8	-	96.0	34.8	-	260.0

However, introducing biomass, which has distinct physical and chemical properties to coal (e.g., higher volatiles, lower fixed carbon and density, different ash composition), can alter the combustion dynamics, heat transfer, and erosion characteristics within a boiler designed specifically for coal [8]. Understanding these changes is of great importance for the safe and efficient operation. Experimental measurements in large-scale industrial CFBs are technically challenging and economically costly, often limited to point measurements that cannot include the full internal state of the reactor.

Computational fluid dynamics (CFD) offers a cost-effective and practical approach for addressing these challenges. A number of CFD studies have been conducted to explore co-combustion in fluidized beds. For instance, researchers have employed the Eulerian–Eulerian (Two-Fluid Model, TFM) approach to investigate the impacts of biomass type and co-firing ratio on combustion efficiency and emissions [9,10]. These studies provided valuable insights but often relied on simplified particle treatments. For more fundamental studies requiring detailed particle-level information, the Combined Computational Fluid Dynamics and Discrete Element Method (CFD-DEM) have been successfully applied. CFD-DEM deals with the particle–particle interaction according to the soft sphere model, which can track real collision between particles [11]. This approach has been used to elucidate mixing/segregation behavior and combustion characteristics of coal and biomass blends for small-scale fluidized beds [12,13]. However, the formidable computational cost of CFD-DEM restricts its application to laboratory-scale systems with a limited number of particles. The number of computational particles is restricted to 2×10^5 particles by CFD-DEM while the actual number of particles in a CFB generally exceeds one billion [14]. The Multiphase Particle-In-Cell (MP-PIC) method is particularly well-suited for simulating industrial-scale multiphase flows like CFBs, as it efficiently models large numbers of particles by parceling them into computational particles, significantly reducing the computational cost compared to Discrete Element Method (DEM) while retaining a Lagrangian framework for the solid phase [15–17]. In the MP-PIC method, the solid phase is described statistically using a particle phase-space distribution function in which the temporal and spatial evolution is governed by the Liouville transport equation. To overcome the enormous computational cost of tracking individual physical particles at industrial scale, numerous identical real particles with consistent size, density and velocity properties are lumped into a single Lagrangian computational parcel, which serves as the fundamental tracking unit to statistically represent the overall solid particle characteristics [18,19]. The inter-particle crowding and dense packing effects in the MP-PIC framework are incorporated as solid stress acceleration terms in the source term of the Liouville equation [19–21]. The coupled Eulerian fluid phase and Lagrangian parcel phase are solved iteratively through bidirectional field mapping, ultimately closing the Eulerian–Lagrangian multiphase flow coupling [19,22].

To address the aforementioned limitations of previous studies and bridge the gap between laboratory-scale simulation and industrial application, as well as to provide reliable theoretical support for the safe, efficient and low-emission operation of industrial CFB boilers co-firing coal and biomass, this study developed a MP-PIC model for an industrial CFB boiler co-firing coal and biomass with experimentally determined pyrolysis kinetics of coal and rice husk. Upon model validation against experimental data, the model will systematically investigate the impact of rice husk biomass-blending ratio (0 wt.%, 10 wt.%, 20 wt.%, 30 wt.%, 40 wt.%) on particle flow, temperature distribution, and emissions of CO_2, NO, and SO_2. The present work strictly restricts its research scope to the fixed blending ratios of rice husk (0–40 wt.%) under identical industrial operating conditions, without extended parametric sensitivity tests or multi-biomass comparative simulations, which will be systematically explored in our subsequent independent studies.

2. Methodology

2.1. Fuel Characterization and Pyrolysis Kinetics

A bituminous coal and rice husk were selected in this study. Their proximate and ultimate analyses are presented in Table 2. Proximate analysis confirmed rice husk had significantly higher volatile matter (59.49 wt.%) and lower fixed carbon (12.96 wt.%) than coal (29.96 wt.% and 41.59 wt.%, respectively). The ultimate analysis showed that N and S in rice husk are one order of magnitude lower than those in coal, which would have significant impact on the pollutant emissions after co-firing. Coal and rice husk samples were crushed and sieved through an 80-mesh sieve. Non-isothermal thermogravimetric analysis (TGA) was conducted at heating rates of 10, 20, and 30 $K \cdot min^{-1}$ under a N_2 atmosphere from room temperature to 1000 °C with a N_2 flowrate of 100 $mL \cdot min^{-1}$. Each sample was tested three times to ensure the reproducibility. TG and DTG data are shown in Figure S6. The iso-conversional method was employed to determine the apparent activation energy (E_a) [23]. The apparent average activation energies for pyrolysis were found to be 240.98 $kJ \cdot mol^{-1}$ for coal and 169.83 $kJ \cdot mol^{-1}$ for rice husk, confirming the biomass is more reactive. A single-step, first-order ($F1$) reaction model was adopted for devolatilization in the simulation. The best fitting decomposition expressions for coal and rice husk are Equations (1) and (2)

$$\frac{d\alpha}{dt} = 8.06 \times 10^{12} \exp\left(-\frac{240984}{RT}\right)(1-\alpha) \quad (1)$$

$$\frac{d\alpha}{dt} = 2.68 \times 10^{12} \exp\left(-\frac{16938}{RT}\right)(1-\alpha) \quad (2)$$

Table 2. Proximate and ultimate analysis of coal and rice husk.

Analysis (wt.%)	Coal	Rice Husk
Proximate (ar)		
Moisture	4.06	5.84
Ash	24.39	21.71
Volatile Matter	29.96	59.49
Fixed Carbon	41.59	12.96
Ultimate (daf)		
Carbon	67.18	34.64
Hydrogen	4.08	4.80

Table 2. *Cont.*

Analysis (wt.%)	Coal	Rice Husk
Oxygen (by diff.)	2.66	38.31
Nitrogen	1.13	0.50
Sulfur	0.56	0.04

2.2. MP-PIC Model Description

The MP-PIC Model was set up to simulate the CFB boiler [24]. The geometry includes a furnace (lower cylindrical section, upper rectangular section), a cyclone separator, an external heat exchanger (EHE), and a loop seal (Figure 1). The boundary conditions were also marked for each part. To balance the computational cost and efficiency, the fluidizing air nozzle was simplified as a flat plate with uniform velocity [25,26].

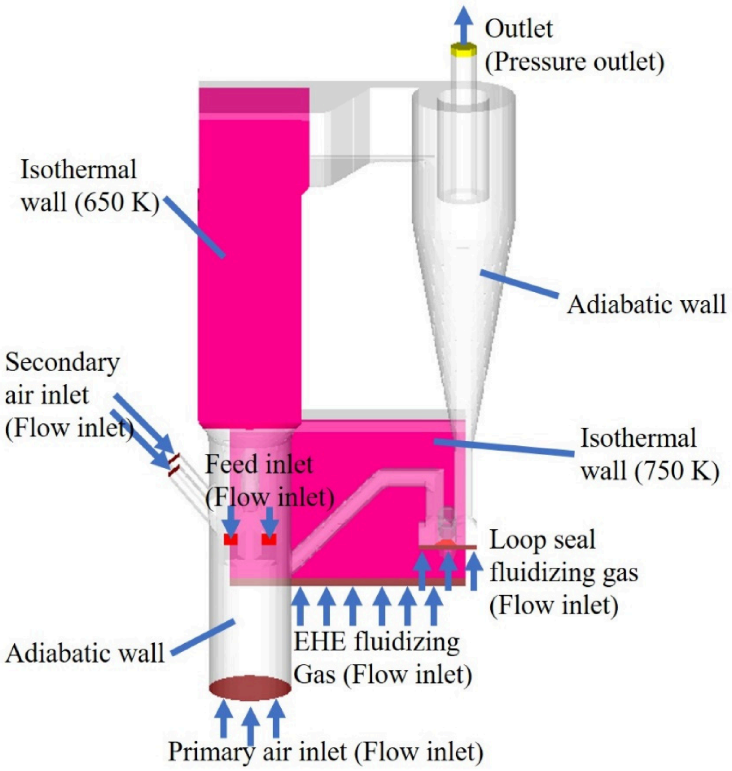


Figure 1. The circulating fluidized bed boiler geometry with marked boundary conditions. (Red: Flow boundary. Yellow: Pressure boundary. Pink: Isothermal wall. Gray: Adiabatic wall. This CFB boiler consists primarily of a furnace, a cyclone separator, an external heat exchanger, and a J-valve. The furnace comprises two sections: the lower section is a cylinder 10 m high with a cross-sectional inner diameter of 3.15 m; the upper section is a rectangular prism 12 m high with a cross-sectional inner diameter of 3.96 m, giving the total furnace height 23.5 m).

The solid phase was solved using the coarse grain model with MP-PIC approach, where particles in the model calculation represented many real particles that have identical properties. The Wen-Yu/Ergun hybrid model was adopted here. The gas–solid momentum exchange across a wide range of solid volume fractions was calculated by [27].

$$\boldsymbol{F}(\varepsilon_s, Re) = \begin{cases} \boldsymbol{F}_{WY} & \varepsilon_s \leq 0.2 \\ \boldsymbol{F}_E & \varepsilon_s > 0.2 \end{cases} \quad (3)$$

The drag force could be expressed as

$$\boldsymbol{f}_{\text{drag}} = \beta(\boldsymbol{u}_{\text{g}} - \boldsymbol{u}_{\text{s}}) \tag{4}$$

where β is the interphase momentum exchange coefficient (drag per unit volume), u_{g} is the gas velocity, and u_{s} is the solid velocity. β depends on the bed density. In high solid volume fraction ($\varepsilon_{\text{s}} \geq 0.2$), Ergun-based drag model is used to compute β [28].

$$\beta_{\text{Ergun}} = \frac{150(1-\varepsilon_{\text{g}})\mu_{\text{g}}}{\varepsilon_{\text{g}} d_{\text{p}}^2} + \frac{1.75\rho_{\text{g}}|u_{\text{g}} - u_s|}{d_{\text{p}}} \tag{5}$$

where ε_{g} is gas volume fraction $(1 - \varepsilon_{\text{s}})$, μ_{g} is gas viscosity, ρ_{g} is gas density and d_{p} is particle size. For lower solid volume fraction situation ($\varepsilon_{\text{s}} < 0.2$), the drag interphase momentum exchange coefficient is based on the particle Reynolds number and drag coefficient for a single particle C_{D} [17,28,29].

$$Re = \frac{\rho_{\text{g}} d_{\text{p}}|u_{\text{g}} - u_s|}{\mu_{\text{g}}} \tag{6}$$

$$C_{\text{D}} = \frac{24}{\text{Re}}\left(1 + 0.15\text{Re}^{0.687}\right) \tag{7}$$

$$\beta_{\text{Wen-Yu}} = \frac{3}{4} C_{\text{D}} \frac{\rho_{\text{g}} \varepsilon_{\text{g}}|u_{\text{g}} - u_s|}{d_{\text{p}}} \varepsilon_{\text{g}}^{-2.65} \tag{8}$$

For heat transfer between gas phase and solid particle phase, fluid-to-particle heat transfer coefficient h_{p} is used to model heat transfer. The general form of the fluid-to-particle heat transfer coefficient is as follows [1,2].

$$h_{\text{p}} = \left(c_0 {Re_{\text{p}}}^{n_1} Pr^{0.33} + c_1\right)\frac{k_{\text{g}}}{d_{\text{p}}} + c_2 \tag{9}$$

where c_0, c_1, c_2, and n_1 are model parameters. k_{g} is the thermal conductivity of the gas, $\text{W}\cdot\text{m}^{-1}\cdot\text{K}^{-1}$. d_p is the particle diameter, m. The Prandtl numbers are defined as [1,2].

$$Pr = \frac{\mu_{\text{g}} C_{\text{p,g}}}{k_{\text{f}}} \tag{10}$$

where $C_{\text{p,g}}$ is the fluid heat capacity, $\text{J}\cdot\text{kg}^{-1}\cdot\text{K}^{-1}$.

The heat transfer between the particle is as follows [1,2].

$$\varepsilon_{\text{p}}\rho_{\text{p}} C_{\text{p}} \frac{\partial T_{\text{p}}}{\partial t} = \nabla \cdot (k_{\text{eff}} \nabla T_{\text{p}}) \tag{11}$$

$C_{\text{p,s}}$ is particle-specific heat, $\text{kJ}\cdot\text{kg}^{-1}\cdot\text{K}^{-1}$. T_{p} is particle temperature, K. k_{eff} is the particle effective thermal conductivity, $\text{W}\cdot\text{m}^{-1}\cdot\text{K}^{-1}$. It is related to the particle volume fraction by the following relation [1,2].

$$k_{\text{eff}} = k_{\text{p}} \frac{3\varepsilon_{\text{p}} - 1}{2} \tag{12}$$

where k_{p} represents the mass-weighted average of thermal conductivities of particle materials, $\text{W}\cdot\text{m}^{-1}\cdot\text{K}^{-1}$.

Another major mode of heat transfer is the radiation between wall and particles. The radiation between them is calculated as [1,2].

$$q_{\text{wp}} = A_{\text{w}} F_{\text{wp}} \alpha_{\text{wp}} \sigma \left({T_{\text{w}}}^4 - {T_{\text{p}}}^4\right) \tag{13}$$

where A_w is the area of the thermal wall, m^2. T_w is the temperature of the wall, K. T_p is particle temperature, K. σ is the Stefan–Boltzmann constant. F_{wp} is view factor. α_{wp} is the effective emissivity between the wall and the particles.

$$\alpha_{wp} = \left(\frac{1}{\alpha_p} + \frac{1}{\alpha_w} - 1 \right)^{-1} \tag{14}$$

where α_p is the particle emissivity and α_w is the specified emissivity of the wall.

2.3. Chemical Reaction Kinetics

A key part of the multiphase model is to incorporate the chemical reaction kinetics. The kinetics of devolatilization of the coal and the rice husk would take the experimentally determined kinetics.

R1 $\text{Coal} \rightarrow a_1\text{Char(s)} + b_1\text{CO} + c_1\text{CO}_2 + d_1\text{CH}_4 + e_1\text{H}_2 + f_1\text{H}_2\text{O} + g_1\text{HCN} + h_1\text{NH}_3 + i_1\text{H}_2\text{S} + j_1\text{Tar} + k_1\text{Ash(s)}$

R2 $\text{Rice hust} \rightarrow a_2\text{Char(s)} + b_2\text{CO} + c_2\text{CO}_2 + d_2\text{CH}_4 + e_2\text{H}_2 + f_2\text{H}_2\text{O} + g_2\text{HCN} + h_2\text{NH}_3 + i_2\text{H}_2\text{S} + j_2\text{Tar} + k_2\text{Ash(s)}$

For rice husk, the nitrogen and sulfur contents are substantially lower than those in coal (N: 0.50 wt.% vs. 1.13 wt.%; S: 0.04 wt.% vs. 0.56 wt.%). Consequently, the stoichiometric coefficients for nitrogen- and sulfur-containing species (g_2, h_2, i_2, j_2, k_2 and f_2 for char-bound N) in R2 are accordingly smaller than their counterparts in R1, particularly for sulfur-containing species where the difference is approximately one order of magnitude. These species are retained in the reaction stoichiometry for formal completeness and mass conservation, though their contributions to the overall NO and SO_2 emissions from rice husk degradation are negligible.

The combustion is assumed to occur after the devolatilization of coal and rice husk. The combustion reactions include char combustion, carbon monoxide combustion, methane combustion, hydrogen combustion and tar combustion.

R3 $\text{C} + \varphi\text{O}_2 \rightarrow (2\varphi - 1)\text{CO}_2 + (2 - 2\varphi)\text{CO}$

R4 $\text{CO} + \frac{1}{2}\text{O}_2 \rightarrow \text{CO}_2$

R5 $\text{CH}_4 + 2\text{O}_2 \rightarrow \text{CO}_2 + 2\text{H}_2\text{O}$

R6 $\text{H}_2 + \frac{1}{2}\text{O}_2 \rightarrow \text{H}_2\text{O}$

R7 $\text{tar} + \text{O}_2 \rightarrow \text{H}_2\text{O} + \text{CO}_2$

Other major gas phase reactions include char steam reforming, Boudouard reaction, and methanation.

R8 $\text{C} + \text{H}_2\text{O} \leftrightarrow \text{CO} + \text{H}_2$

R9 $\text{C} + \text{CO}_2 \leftrightarrow 2\text{CO}$

R10 $\frac{1}{2}\text{C} + \text{H}_2 \leftrightarrow \frac{1}{2}\text{CH}_4$

Burning coal and biomass together produces pollutants, among which NOx is a typical pollutant. Nitrogen-containing volatile substances in coal and biomass are preferentially released as HCN and NH_3 during pyrolysis and volatilization. HCN can quickly convert into an intermediate product, CNO, which further reacts with O_2 to produce NO or reacts with NO to form N_2O. NH_3, in the presence of sufficient O_2, can directly react with O_2 and be converted into NO. The carbon (C) concentration in the reactor is very important because NO can be reduced to N_2.

R11 $$HCN + \frac{3}{4}O_2 \rightarrow CNO + \frac{1}{2}H_2O$$

R12 $$CNO + \frac{1}{2}O_2 \rightarrow NO + CO$$

R13 $$CNO + NO \rightarrow N_2O + CO$$

R14 $$N_2O \rightarrow N_2 + \frac{1}{2}O_2$$

R15 $$N_2O + CO \rightarrow N_2 + CO_2$$

R16 $$NH_3 + \frac{3}{4}O_2 \rightarrow \frac{1}{2}N_2 + \frac{3}{2}H_2O$$

R17 $$NH_3 + \frac{5}{4}O_2 \rightarrow NO + \frac{3}{2}H_2O$$

R18 $$NO + NH_3 + \frac{1}{4}O_2 \rightarrow N_2 + \frac{3}{2}H_2O$$

R19 $$NO + C \rightarrow \frac{1}{2}N_2 + CO$$

R20 $$NO + \frac{1}{2}C \rightarrow \frac{1}{2}N_2 + \frac{1}{2}CO_2$$

R21 $$NO + CO \rightarrow \frac{1}{2}N_2 + CO_2$$

Similar to NOx, SO_2 is also a common pollutant during the co-combustion. During the pyrolysis and volatilization process, volatile sulfur is released in the form of H_2S and SO_2. In the combustion process, flue gas contacts the ash, which contains CaO, to form calcium sulfate. The chemical reactions are as follows [30,31]:

R22 $$H_2S + \frac{3}{2}O_2 \rightarrow SO_2 + H_2O$$

R23 $$CaO + SO_2 + \frac{1}{2}O_2 \rightarrow CaSO_4$$

The reaction rates of the above reactions are summarized in Table 3.

Table 3. Summary of reaction rates and rate coefficients.

Reaction No.	Reaction Rate, r (kmol·m^{-3}·s^{-1})	Rate Coefficient, k [14,24,30,32–38]
R1	$r_1 = k_1 C_{\text{volatile}}$	$k_1 = 8.06 \times 10^{12} \exp(-\frac{28985}{T})$
R2	$r_2 = k_2 C_{\text{volatile}}$	$k_2 = 2.68 \times 10^{12} \exp(-\frac{20427}{T})$
R3	$r_3 = k_3 C_{O_2}$	$k_3 = 4.43 \times 10^7 \theta_c T \exp(-13592/T)$
R4	$r_4 = k_4 C_{CO} C_{O_2}$	$k_4 = 5.62 \times 10^{12} \exp(-16000/T)$
R5	$r_5 = k_5 C_{CH_4} C_{O_2}$	$k_5 = 3.552 \times 10^{14} \exp(-15700/T) T^{-1}$
R6	$r_6 = k_6 C_{H_2}^{1.5} C_{O_2}$	$k_6 = 1.63 \times 10^{11} \exp(-3430/T) T^{-1.5}$
R7	$r_7 = k_7 C_{Tar} C_{O_2}$	$k_7 = 3.8 \times 10^7 \exp(-6675/T)$
R8	$r_{8a} = k_{8a} C_{H_2O}$ $r_{8b} = k_{8b} C_{CO} C_{H_2}$	$k_{8a} = 1.272 m_s T \exp(-22645/T)$ $k_{8b} = 1.044 \times 10^{-4} m_s T^2 \exp(-6319/T - 17.29)$
R9	$r_{9a} = k_{9a} C_{CO_2}$ $r_{9b} = k_{9b} C_{CO}^2$	$k_{9a} = 1.272 m_s T \exp(-22645/T)$ $k_{9b} = 1.044 \times 10^{-4} m_s T^2 \exp(-6319/T - 17.29)$
R10	$r_{10a} = k_{10a} C_{H_2}$ $r_{10b} = k_{10b} C_{CH_4}^{0.5}$	$k_{10a} = 1.368 \times 10^{-3} m_s T \exp(-8078/T - 7.087)$ $k_{10b} = 0.151 m_s T^{0.5} \exp(-13578/T - 0.372)$
R11	$r_{11} = k_{11} C_{HCN} C_{O_2}$	$k_{11} = 2.14 \times 10^8 \exp(-10000/T)$
R12	$r_{12} = k_{11} C_{HCN} C_{O_2} \frac{k_{12a}}{k_{12a} + k_{12b} C_{NO}}$	$\frac{k_{12b}}{k_{12a}} = 1.02 \times 10^{12} \exp(-25460/T)$
R13	$r_{13} = k_{11} C_{HCN} C_{O_2} \frac{k_{13b} C_{NO}}{k_{13a} + k_{13b} C_{NO}}$	$\frac{k_{13b}}{k_{13a}} = 1.02 \times 10^{12} \exp(-25460/T)$
R14	$r_{14} = k_{14} C_{N_2O}$	$k_{14} = 1.5 \times 10^{11} \exp(-20158/T)$
R15	$r_{15} = k_{15} C_{N_2O} C_{CO}$	$k_{15} = 1.24 \times 10^9 \exp(-5913/T)$

Table 3. *Cont.*

Reaction No.	Reaction Rate, r (kmol·m^{-3}·s^{-1})	Rate Coefficient, k [14,24,30,32–38]
R16	$r_{16} = k_{16}\frac{C_{NH_3}C_{O_2}}{C_{O_2}+k'}$	$k_{16} = 3.38 \times 10^7 \exp(-10000/T)$ $k' = 0.054$
R17	$r_{17} = k_{17}C_{NH_3}C_{O_2}$	$k_{17} = 3.1 \times 10^8 \exp(-10000/T)$
R18	$r_{18} = k_{18}C_{NO}^{0.5}C_{NH_3}^{0.5}C_{O_2}^{0.5}$	$k_{18} = 1.1 \times 10^{12} \exp(-27680/T)$
R19	$r_{19} = k_{19}C_{NO}$	$k_{19} = 1.5 \times 10^8 \exp(-12000/T)d_s^{-1}$
R20	$r_{20} = k_{20}C_{NO}$	$k_{20} = 3.3 \times 10^5 \exp(-17111/T)d_s^{-1}$
R21	$r_{21} = k_{21}\left[\frac{aC_{NO}(bC_{NO}+c)}{aC_{NO}+bC_{NO}+c}\right]$	$k_{21} = 1.95 \times 10^7 \exp(-19000/T_g)$ $a = 182.6$ $b = 7.86$ $c = 0.002531$
R22	$r_{22} = k_{22}C_{H_2S}^{0.2}C_{O_2}^{1.3}$	$k_{22} = 2.12 \times 10^{11} \exp(-24500/T)$
R23	$r_{23} = \frac{\varepsilon_s\rho_s Y_{CaO}}{\rho_{CaO}}\eta k_{23}C_{SO_2}$	$k_{23} = 1.1 \times 10^6 \exp(-7157/RT)$ $\eta = \exp(-5.71X)$ $X = \frac{C_{CaSO_4}}{C_{CaO}+C_{CaSO_4}}$

This model employs a particle-resolved, lattice Boltzmann-based CFD solver combined with Discrete Element Method (DEM) for particle interactions. Turbulence was modeled using the default LES (Large Eddy Simulation) turbulence model in CPFD Barracuda. Radiation was incorporated into the thermal analysis. The P-1 radiation function of CPFD Barracuda was enabled throughout the simulations. The particle size distribution for coal and ash in this model was shown in Figures S2–S5.

2.4. Mesh Independent Study and Model Validation

To ensure the model results are independent of the grid system used, three different mesh systems were tested, consisting of 85,700, 101,200, and 125,300 cells, respectively. Solid mass flux at different heights, temperature distribution and outlet gas molar fractions were extracted from the results to test the mesh independence. As shown in Figure 2, when the mesh size exceeded 101,200 cells, the solid mass flux and temperature, as well as the gas mole fraction at the outlet of the cyclone separator, exhibit minimal variation, with a maximum deviation of less than 1%. Generally, a finer mesh yielded closer value to analytical solution but also increased computational cost. To balance accuracy and computational efficiency, a mesh size of 101,200 cells was selected throughout this study.

Initial and boundary conditions for model validation were set according to industrial data (Table 4 and Figure S1). The simulation ran for 30 s of physical time, with time-averaged data collected from 25 to 30 s after quasi-steady state was achieved. The model was rigorously validated against industrial results for solid mass flux, temperature distribution across the furnace, and gas species concentrations (O_2, CO_2, NO, SO_2) at the cyclone outlet. The alignment with the experimental data confirmed the model's accuracy and reliability.

Table 4. Key simulation input parameters.

Parameter	Value
Primary Air Flow (kg·s^{-1})	9.32
Primary Air Temperature (K)	449
Secondary Air Flow (kg·s^{-1})	17.8
Secondary Air Temperature (K)	449

Table 4. *Cont.*

Parameter	Value
EHE Gas Flow ($kg \cdot s^{-1}$)	0.35
EHE Gas Temperature (K)	698
Loop Seal Flow ($kg \cdot s^{-1}$)	0.30
Loop Seal Flow Temperature (K)	1100
Coal/Biomass Feed Rate ($kg \cdot s^{-1}$)	2.98
Feed Air Flow ($kg \cdot s^{-1}$)	1.89
Feed Temperature (K)	321.7
Bed Material	Sand
Bed Material Density ($kg \cdot m^{-3}$)	2650
Operating Pressure (atm)	1
Water Cooled Wall Temperature (K)	650
EHE Wall Temperature (K)	750
Initial Time Step (s)	1×10^{-4}

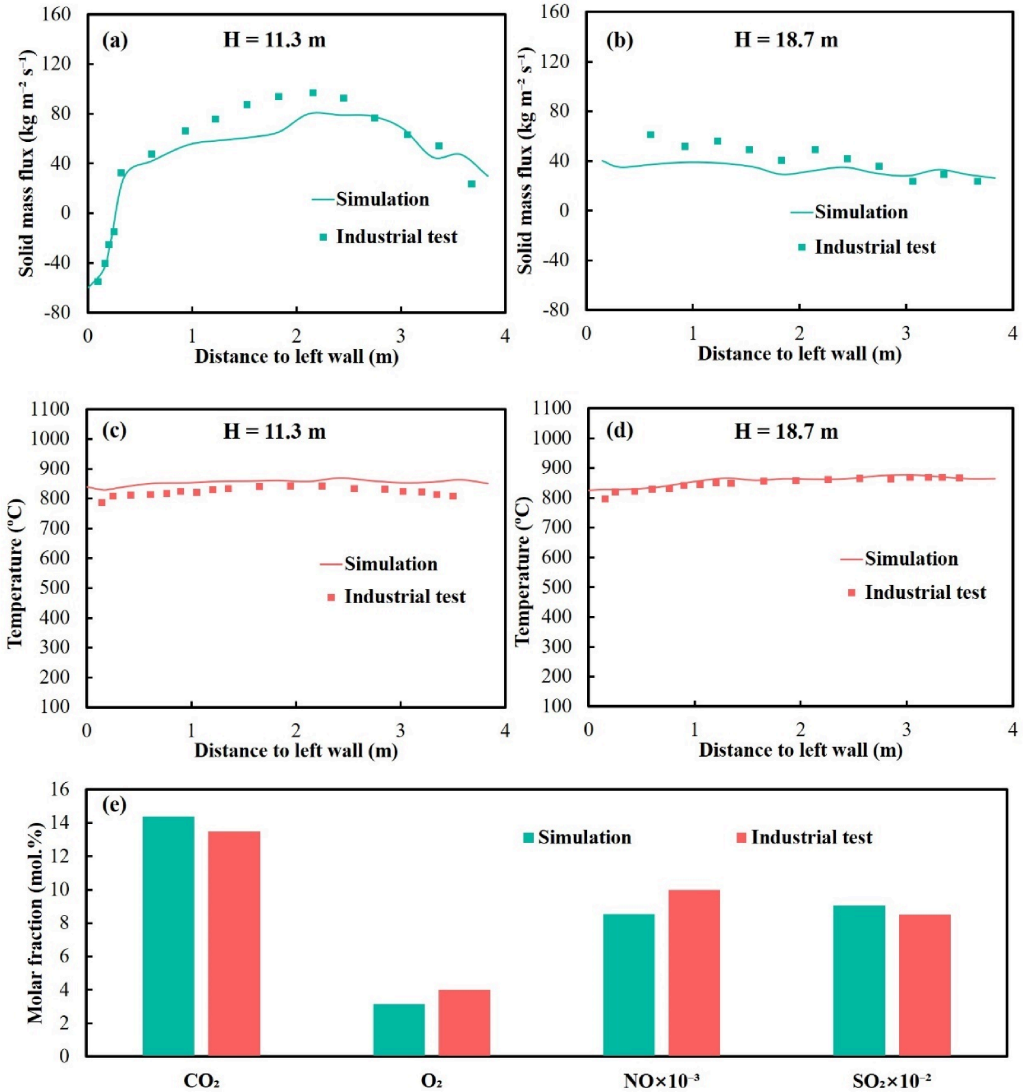


Figure 2. Comparison of simulation data and industrial test data. (**a**) Solid mass flux at H = 11.3 m; (**b**) Solid mass flux at H = 18.7 m. (**c**) Temperature at H = 11.3 m. (**d**) Temperature at H = 18.7 m. (**e**) Gas molar fraction at outlet. The industrial data is from [24].

3. Results and Discussion

3.1. Granular Flow Hydrodynamics

In this simulation, the particle and parcel statistic information are summarized in Supplementary Material. The temporal flow process of particles in the fluid bed is similar regardless of the biomass-blending ratio. During the initial simulation period (0–2 s), particles originally accumulated at the bottom of the furnace, external heat exchanger (EHE), and return leg are fluidized and lifted upward by the primary air (for the furnace), fluidizing air for the EHE, and fluidizing air for the return leg, respectively. From the 2nd to the 4th second of the simulation, particles in the fluidized bed flow upward under the combined action of primary and secondary air. By the 4th second, particles are present throughout the entire furnace. As particle flow continues, by the 10th second of simulation, the entire cyclone separator is also filled with particles, and the particle distribution in the furnace becomes relatively uniform. When the simulation time reaches the 16th second, particles begin to return from the return leg to the fluidized bed, and the complete circulation loop is established. After the 20th second, only minor changes occur in the particle flow within the connecting pipe between the return leg and the fluidized bed. After the 25th s, the particle flow in the CFB boiler reached a quasi-steady state across the entire system. Parameters such as particle volume fraction and temperature during the period from the 25th s to the 30th s were averaged for statistical analysis. During this averaging period (25–30 s), particles in the entire CFB system (except the EHE) exhibit a fast-flowing state, while particles in the EHE show a bubbling flow state—this is consistent with real-world operating conditions.

However, compared with 100 wt.% coal combustion, when biomass was co-fired with coal in the existing coal-fired CFB boiler at different blending ratios (10–40 wt.%), particles showed slightly more accumulation at the leg of the cyclone separator. A possible reason for this is that biomass has lower density than coal. Although adding biomass exerts a certain impact on particle flow inside the furnace, the impact is minimal. This is because, whether biomass is added or not, bed material particles can still circulate and flow relatively uniformly throughout the entire furnace, dwarfing the contribution of the fuel particles.

The above results qualitatively analyze the distribution and flow of particles throughout the circulating fluidized bed. To further understand the distribution and flow conditions of particles in the circulating fluidized bed, a quantitative analysis of particle volume fraction and particle flow velocity is conducted. Even though particle flow is an instantaneous state that varies with time, from the above analysis results between 25 and 30 s, the particle flow in the circulating fluidized bed exhibits a quasi-steady state. The particle flow conditions change little over time. Therefore, the particle volume fraction and flow velocity within this 5 s interval are averaged to obtain the mean particle volume fraction and mean particle velocity, which are then quantitatively analyzed. This approach reduces errors caused by flow variations at a single moment.

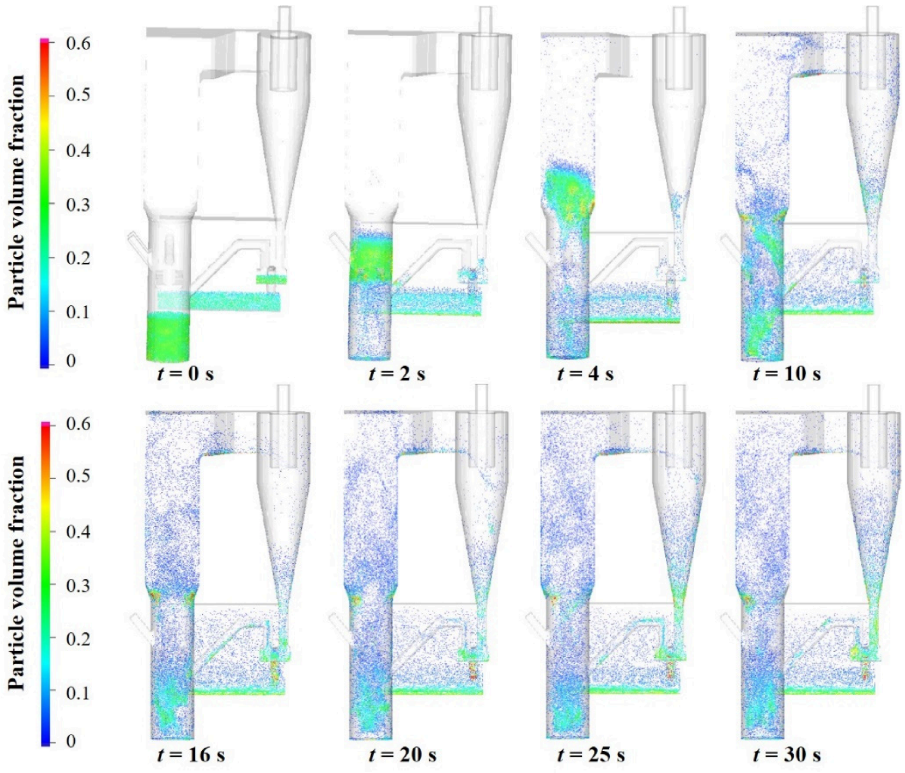
Figure 3 shows the average particle volume fraction at different heights within the fluidized bed when 0 wt.%, 10 wt.%, 20 wt.%, 30 wt.%, and 40 wt.% of biomass is added. Regardless of whether biomass is added, or how much biomass is added relative to coal for co-firing, the trend of the average particle volume fraction with height in the furnace is consistent.

At the bottom of the furnace (0–4 m), the average particle volume fraction changes gradually with increasing height, indicating a relatively uniform distribution of particles at the bottom. The average particle volume fraction here is relatively high, about 0.05, mainly because a large number of particles from the return system are fed back into the furnace.

At heights of 4–5 m, the average particle volume fraction first increases then decreases with height, reaching a peak around 4.5 m at approximately 0.15. The main reason for

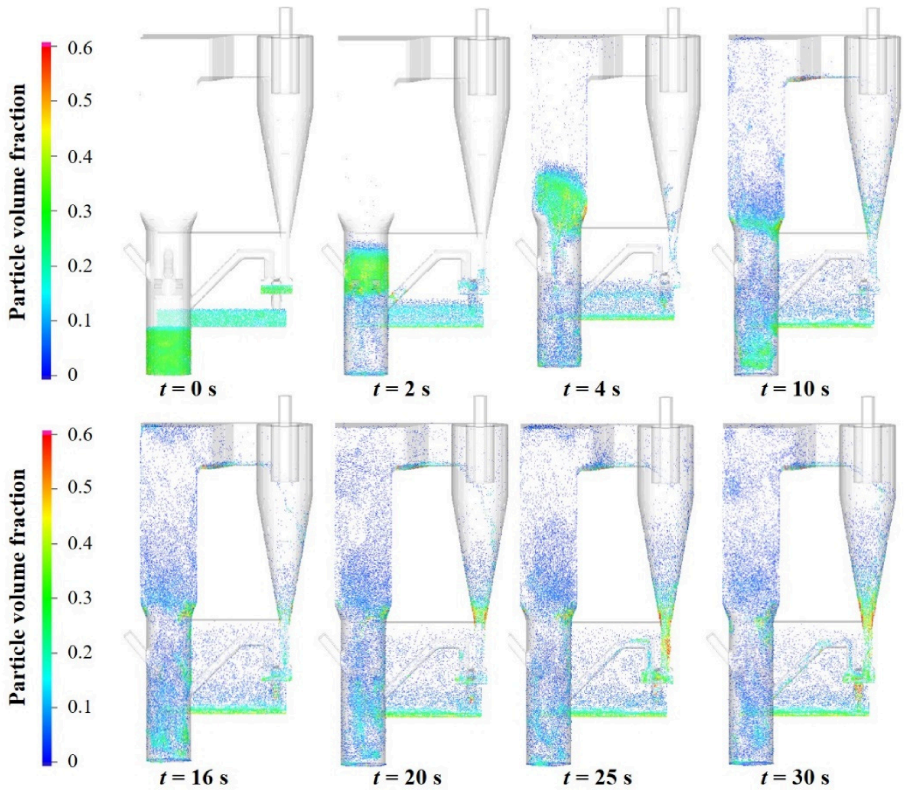
this peak is that two secondary air inlets, inclined downward at 45° above this position, continuously blow secondary air downward, while primary air is blown upward from the bottom. These two air flows cause a large amount of particles from the return system to be compressed here, resulting in a high average particle volume fraction at this location. At heights of 5–10 m, the average particle volume fraction is about 0.02, as there are no additional particles supplied from the return system in this region, so fewer particles are present. The average particle volume fraction increased again, reaching a maximum of about 0.25 around 10.5 m. This is because the upper part of the circulating fluidized bed has a rectangular structure, while the lower part is cylindrical. The rectangular section's cross-sectional diameter is larger than that of the cylinder below, causing falling particles from the upper rectangular section to accumulate at the junction between the two sections. The height of about 10.5 m corresponds to this junction, so the average particle volume fraction peaks here, which aligns with practical observations. Beyond 11.5 m, the average particle volume fraction reaches its lowest point, about 0.006. The above results indicate that adding biomass at any ratio does not alter the original distribution characteristics of particles in the circulating fluidized bed furnace. This is likely because the quantity of biomass particles is far less than that of the existing bed material in the furnace, so their influence on the particle distribution in the bed is minimal.

Figure 4 shows the average particle velocity in axial direction at different heights within the furnace cross-section. The results indicate that, similar to the impact of biomass addition on the average particle volume fraction, regardless of whether biomass is added or how much is added, the general trend of the average axial particle velocity with increasing furnace height does not change significantly.

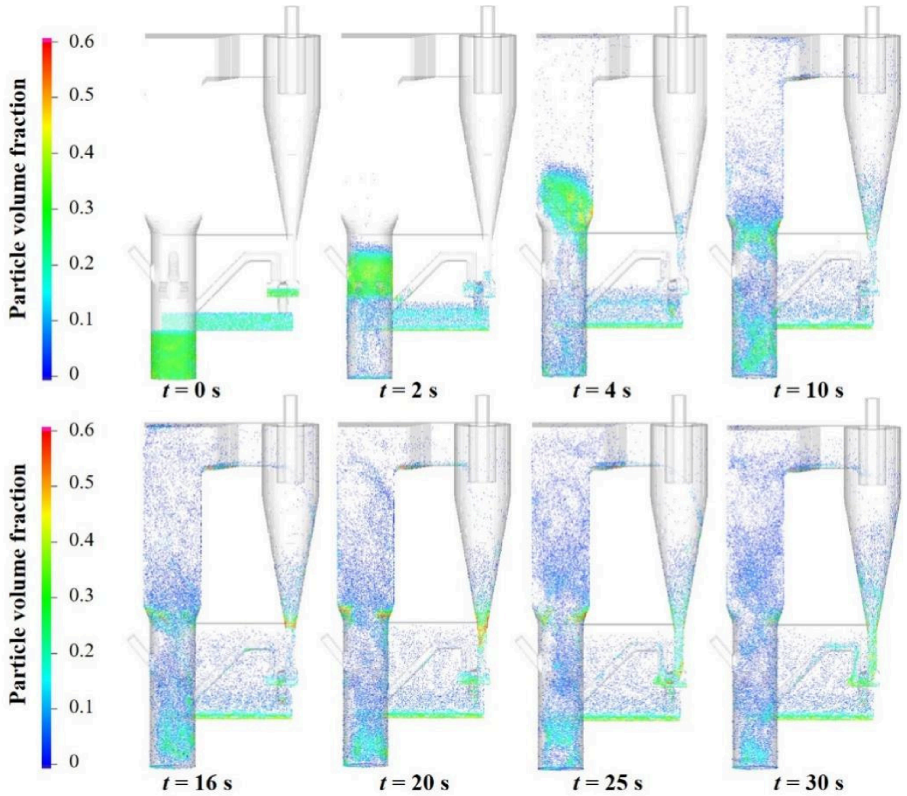


(**a**)

Figure 3. *Cont.*

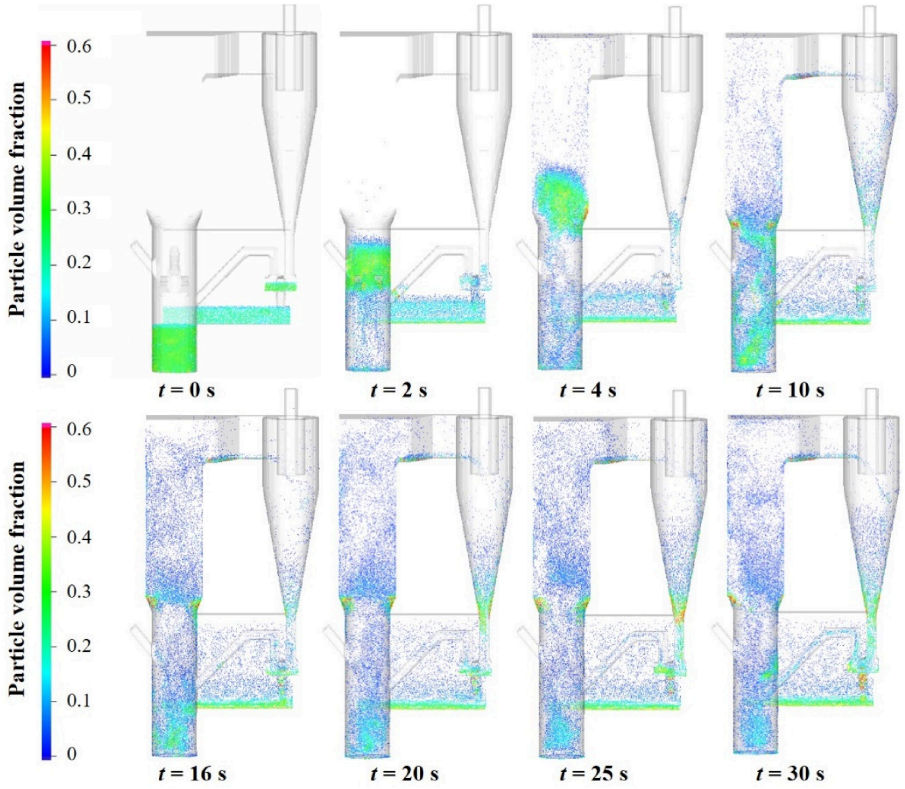


(**b**)

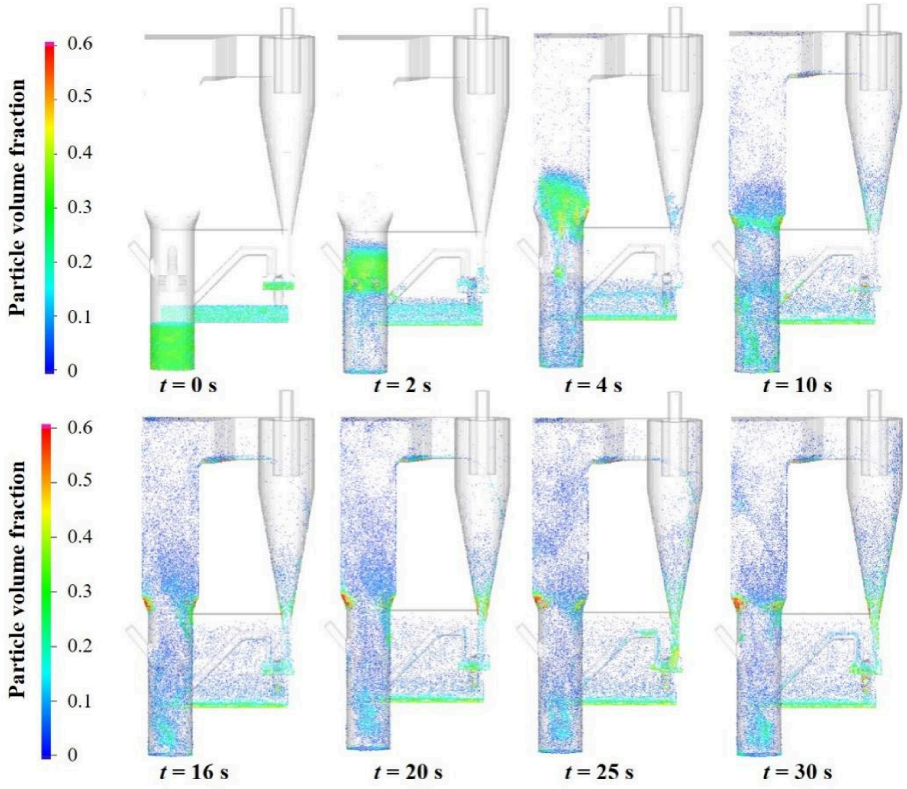


(**c**)

Figure 3. *Cont.*



(**d**)



(**e**)

Figure 3. Flow process of particles with time in circulating fluidized bed with different biomass ratios. The biomass ratio is (**a**) 0 wt.%, (**b**) 10 wt.%, (**c**) 20 wt.%, (**d**) 30 wt.%, (**e**) 40 wt.%.

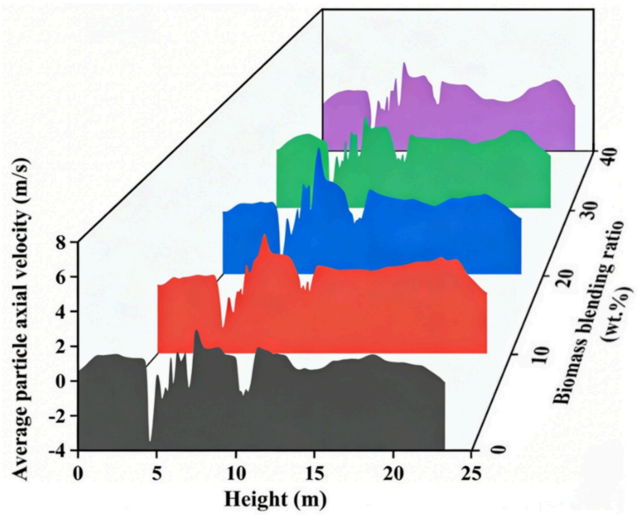


Figure 4. Profile of axial average particle velocity in furnace with different biomass ratios.

Below 4 m of the furnace height, the velocity is relatively high here, about 1.5 m·s^{-1}. This is because a large amount of primary air is blown in from the bottom of the fluidized bed, carrying particles from the lower part of the furnace upward at high speed. When the furnace height reaches about 4.5 m, the average axial velocity suddenly drops sharply to −3.5 m·s^{-1}. This indicates that particles are flowing downward rather than upward here. This is due to the downward secondary air inlet above this point and the return system particles being inclined downward into this region. From 5 m to 8 m in height, the average axial velocity fluctuates significantly but generally increases. The reason for the upward fluctuation is that particles are continuously being blown in from the return system and secondary air, counteracting negative impacts. Between 8 m and 10 m, the average axial velocity is fairly uniform at about 1.9 m·s^{-1}. This is because the particle volume fraction distribution here is uniform (see Figure 5). The above analysis indicates that adding biomass to coal-fired boilers has little effect on the distribution and flow of particles in the furnace. Therefore, adding biomass to circulating fluidized bed furnace does not significantly alter the original distribution and flow characteristics of particles in the bed.

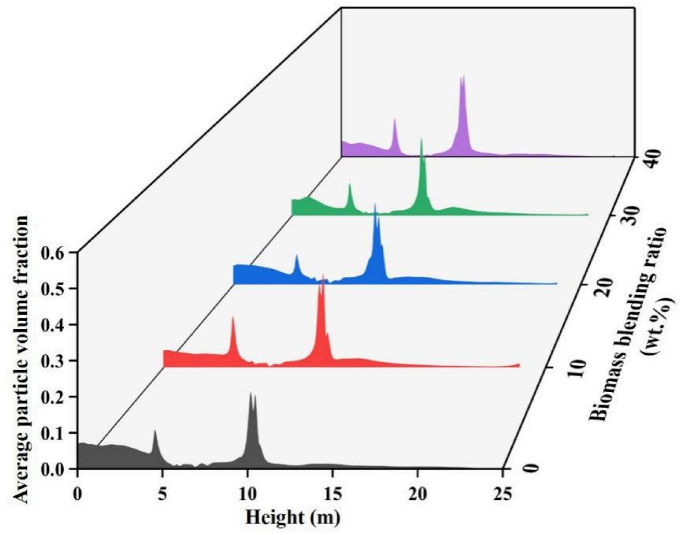


Figure 5. Average particle volume fraction with furnace height at different biomass ratios.

3.2. Temperature Distribution

Figure 6 shows the distribution of gas phase temperature within the circulating fluidized bed under different biomass blending ratios. Regardless of whether biomass is added to the coal-fired circulating fluidized bed, the temperature distribution throughout the bed is similar. Since the secondary air blown in is low-temperature air, the temperature close to the secondary air inlet is relatively low, around 450 K. In the 5–10 m height region, the temperature is higher, reaching about 1150 K. The secondary air injected promoted complete combustion and heat release of coal and biomass, resulting in relatively higher temperatures in this area [39].

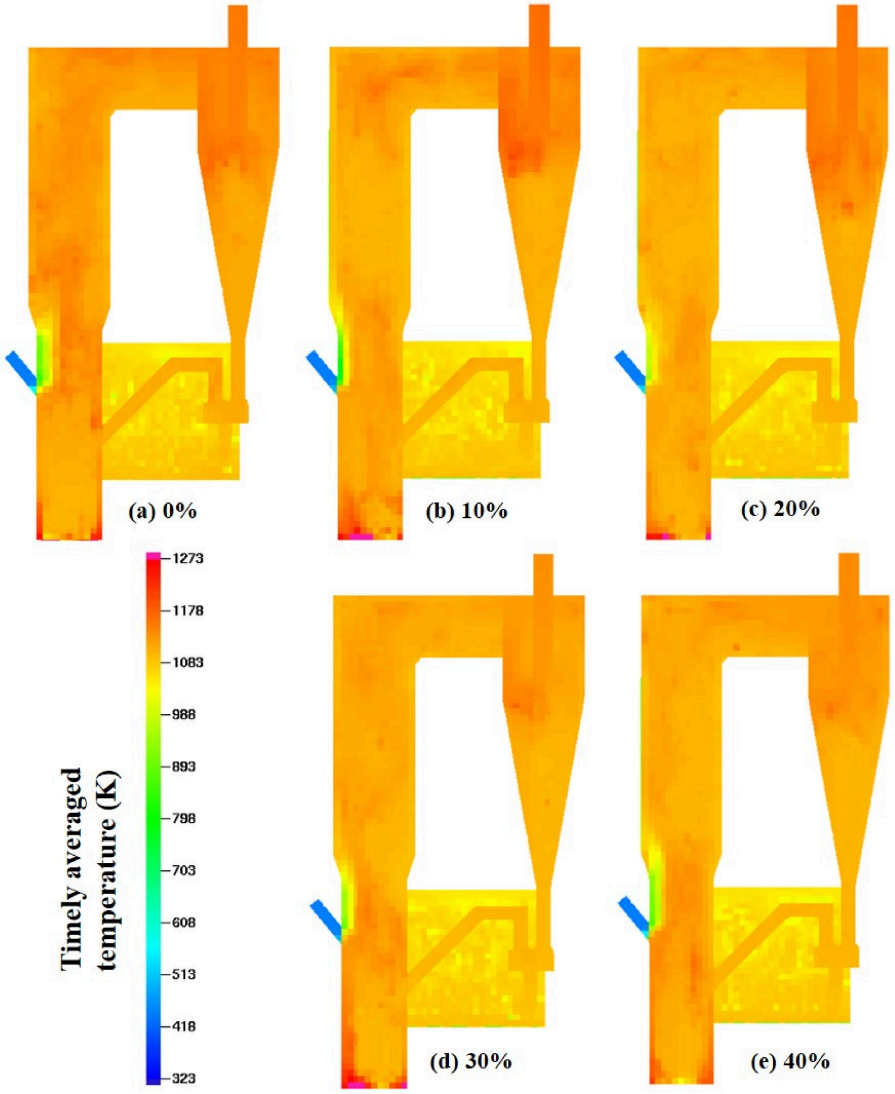


Figure 6. Temperature distribution in circulating fluidized bed boilers at different biomass ratios.

However, as the biomass ratio added to the coal-fired circulating fluidized bed varies, the temperatures in the furnace and cyclone separator change accordingly. As shown in Figure 7, when the biomass ratio increases from 0 wt.% to 40 wt.%, the average temperature of the furnace decreases steadily. Specifically, when the biomass ratio increases from 0 wt.% to 10 wt.%, the average furnace temperature drops significantly from 1145 K to 1132 K, a decrease of 13 K. This is the result of the lower calorific value of biomass. When the biomass ratio increases from 20 wt.% to 40 wt.%, although the average furnace temperature continues to decrease, the reduction is only about 3 K, which is a minor decrease. The increase in biomass-blending ratio does not significantly change the temperature distribution

inside the furnace but mainly reduces the average temperature. For co-firing system with biomass, slagging is a serious concern for the system operation due to the richness of K, Na and relatively lower melting temperature of biomass ash. Even though the reduced temperature is unfavorable from a thermal perspective, such as providing heat or steams in industry, the reduced temperature could favor the durability of the co-firing system by less slagging [40].

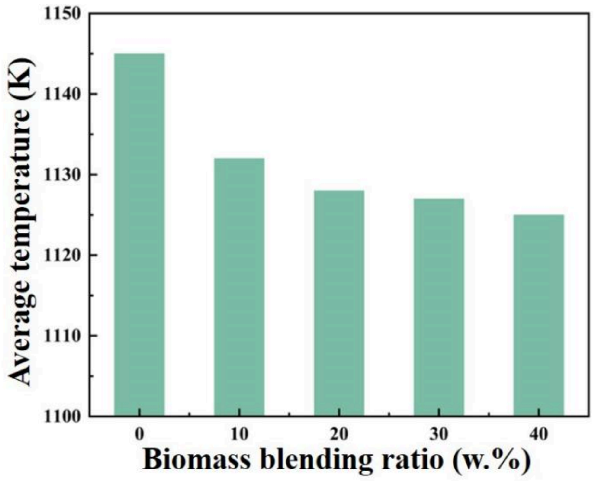


Figure 7. Average furnace temperature at different biomass ratios.

3.3. Distributions of Major Gases

Figures 8 and 9 depicted the molar fraction distributions of O_2 and CO_2 within the CFB under various biomass-blending ratios. At the secondary air inlet, the O_2 molar fraction is particularly high, being approximately 21%, while CO_2 fraction levels are minimal, close to zero. This phenomenon primarily resulted from the continuous influx of oxygen at the secondary air inlet. Due to the sideway gas injection, there is no particle flow at this location. As a result, combustion reactions involving coal and biomass did not proceed, leading to high O_2 and very low CO_2 concentrations. At the bottom of the furnace (approximately 0–2 m), after co-firing biomass with coal, the molar fraction of O_2 ranged from about 10% to 15%, and CO_2 fraction ranged from 5% to 10%. The relatively high CO_2 content in this region indicated that here is one of the primary combustion regions where coal and biomass burnt. In addition, the significant input of primary air at the furnace bottom contributes to the higher O_2 concentrations. As the height increased toward the lower end of the secondary air inlet (approximately 2–7 m), O_2 molar fractions dropped significantly, while CO_2 levels rose, indicating that this region is the main combustion zone.

Above the secondary air inlet (7–23 m), O_2 concentrations on the left side (near the secondary air inlet) are higher than those on the right side (near the cyclone separator), with the opposite trend observed for CO_2. This asymmetry was because the secondary air was only introduced on the left side, which directed more coal and biomass particles toward the right side of the boiler. These particles consumed O_2 and generated CO_2, leading to uneven distribution. Furthermore, with increasing biomass-blending ratio from 0 wt.% to 40 wt.%, O_2 concentration on this side tended to rise, while CO_2 levels declined, reflecting the lower carbon content in biomass compared to coal.

The biomass-blending ratio influenced CO_2 distribution in this zone. Precisely, when 10 wt.% biomass is added to coal, CO_2 levels increased sharply, likely due to the synergistic effect of co-firing, which enhanced combustion efficiency and reduced unburned coke in the particles [41]. As shown in Figure 6, increasing biomass from 0 wt.% to 10 wt.% resulted in higher temperatures, consistent with more complete combustion. However, further

increasing biomass from 10 wt.% to 40 wt.% causes CO_2 levels in this region to decrease progressively, primarily because biomass contains less coke than coal.

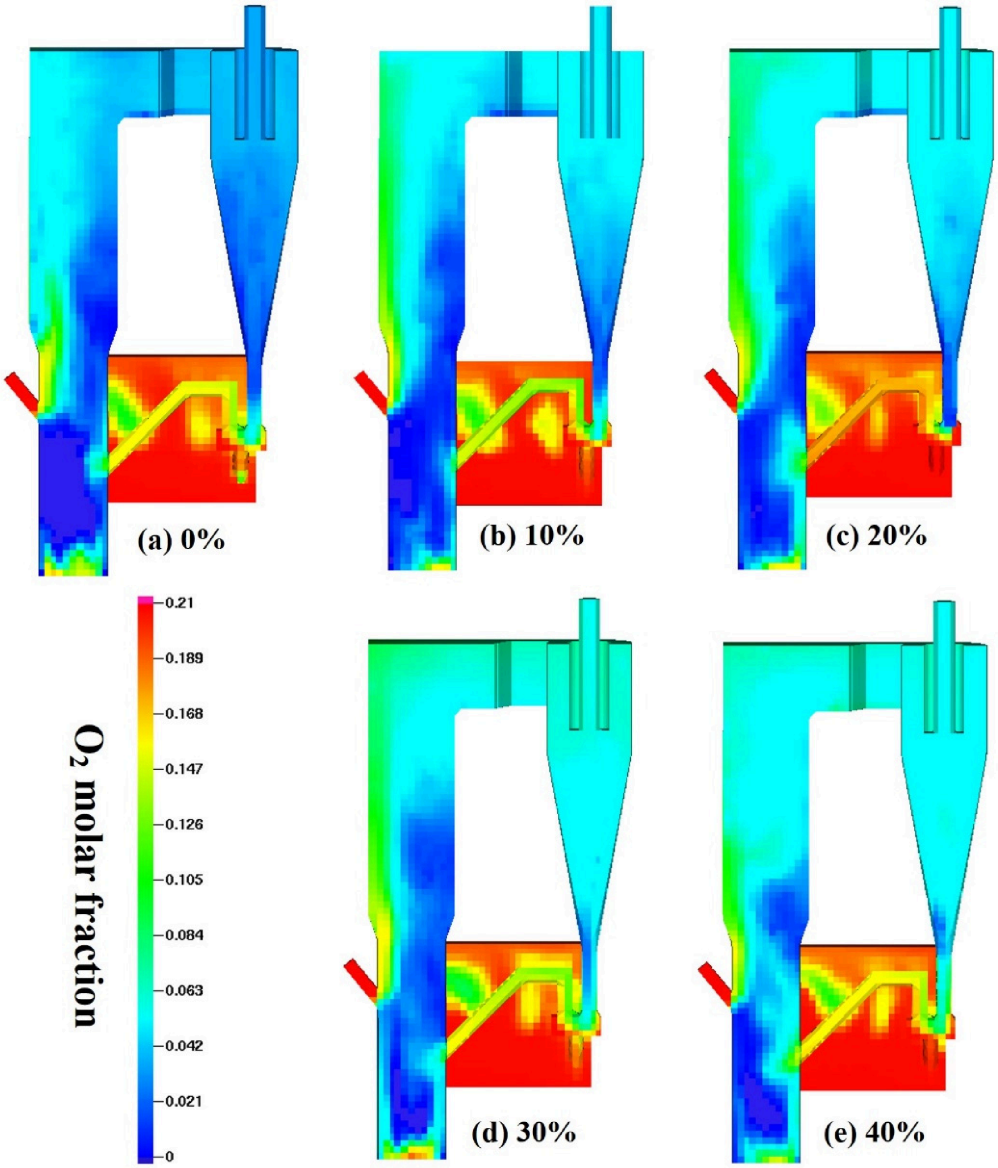


Figure 8. O_2 molar fraction distribution in circulating fluidized bed boilers at different biomass ratios.

Figures 10 and 11 demonstrate that the primary regions for NO and SO_2 generation are within the furnace and cyclone separator, with concentrations higher in the furnace than in the separator. Virtually no NO or SO_2 formation occurs in the return leg, loop, or external heat exchangers. NO primarily results from the oxidation of volatile nitrogen species such as NH_3 and HCN present in coal and biomass particles, while SO_2 mainly originates from the oxidation of volatile sulfur compounds like H_2S. Additionally, some SO_2 generated is absorbed by calcium oxide (CaO) to form calcium sulfate ($CaSO_4$), thereby reducing SO_2 levels within the circulating fluidized bed. Since the formation of NO and SO_2 is driven by the volatilization and oxidation of volatile nitrogen and sulfur in the particles, it can be inferred that once coal and biomass particles enter the furnace through the feed inlet, most begin volatilizing and oxidizing immediately. Consequently, NO and SO_2 concentrations are highest within the furnace, with a smaller portion carried to the cyclone separator for continued volatilization and oxidation. By the time particles reach the return leg, most volatile components have been emitted.

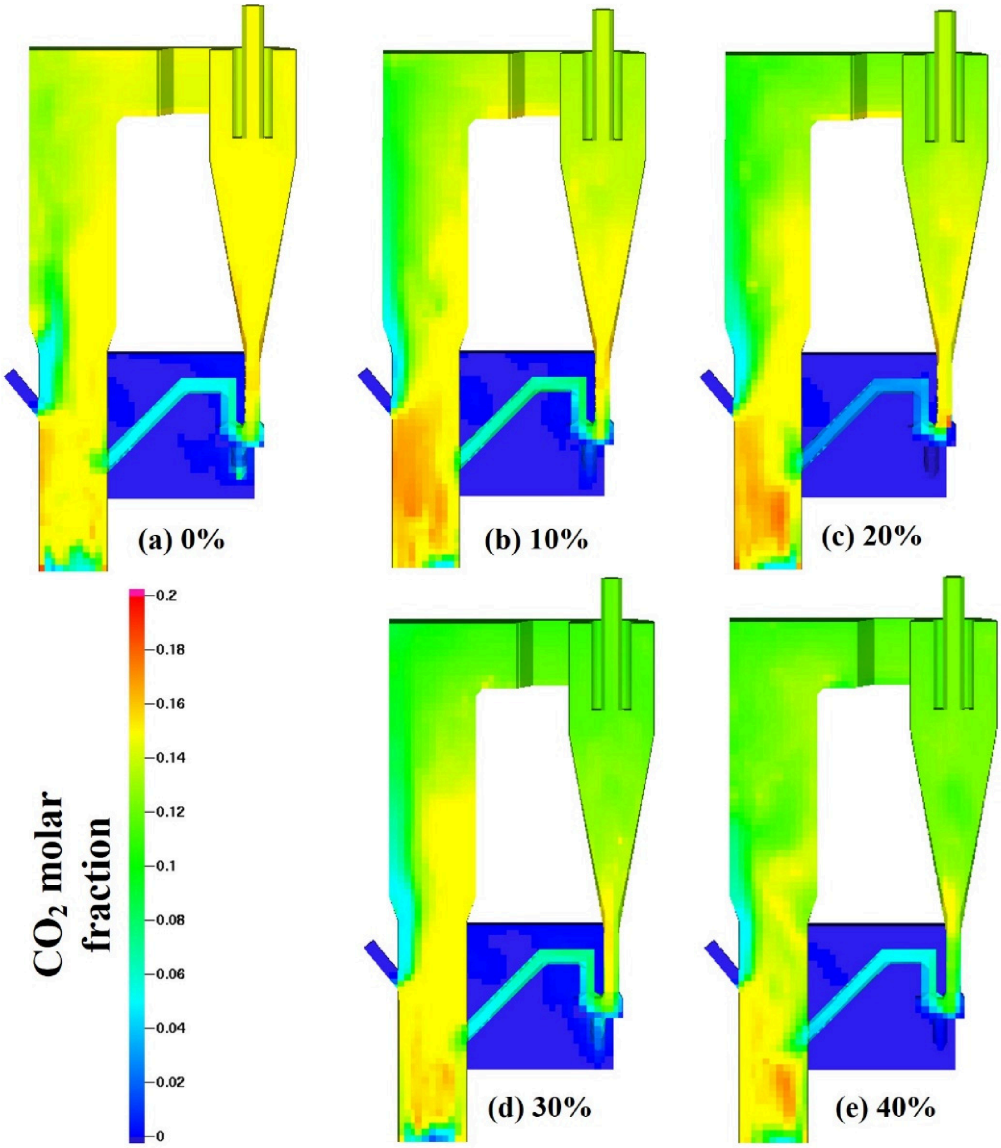


Figure 9. CO_2 molar fraction distribution in circulating fluidized bed boilers at different biomass ratios.

Comparing Figures 8 and 10 revealed that, under the same biomass ratios, regions with higher O_2 concentrations corresponded to higher NO levels. For instance, the lower parts of the furnace exhibited lower O_2 and NO concentrations, whereas the upper parts of the cyclone separator showed higher values. This suggested that O_2 concentration is a critical limiting factor for NO formation in most regions. Increased O_2 tended to promote NO production. However, exceptions also exist, such as the scenario without biomass addition, where the O_2 concentration on the left side of the furnace at 7–23 m is higher than on the right, yet NO levels were elevated on both sides. When biomass reached 40 wt.%, O_2 concentrations are high in both upper and lower parts of the cyclone separator, but NO levels are significantly higher in the upper section. This indicates that at high O_2 levels, the limiting factor shifted from oxygen availability to the nitrogen content, specifically the volatile nitrogen in the particles.

Figure 12 shows that the NO molar fraction at the cyclone outlet rose from 8.53×10^{-5} to 9.86×10^{-5} (an increase of 15.64%), while O_2 molar fractions increased from 3.13% to 4.74% (a 44.74% increase), when biomass-blending increased from 0 wt.% to 10 wt.%. With low biomass blending, the limiting factor for NO formation is O_2, owing to the high volatile nitrogen content and relatively low O_2 levels. So, the slight increase in NO with

10 wt.% blending is due to the increased O_2. As biomass increased beyond 10 wt.%, O_2 levels at the cyclone outlet continued to rise (by 30.91%), but NO molar fractions decreased by 27.10%. This shift indicated that at higher biomass blending, the abundance of volatile nitrogen becomes the primary limiting factor for NO formation (Table 2), as O_2 is no longer the limiting factor. In addition, the reduced temperature also decelerates the rate of NO formation because the activation energy for NO forming is positive (Table 3: R11–13, 17). Figure 11 illustrates that, with increasing biomass, SO_2 concentrations within the furnace and cyclone separator decrease continuously. As shown in Figure 12, increasing biomass from 0 wt.% to 40 wt.% reduces the SO_2 molar fraction at the cyclone outlet from 9.068×10^{-4} to 4.579×10^{-4}, representing a 49.5% reduction. Unlike NO, SO_2 formation is not primarily limited by O_2 availability; rather, it is constrained by the sulfur content in the fuel (according to R22 and Table 2). Biomass generally contains significantly less sulfur than coal [42,43], so higher biomass ratios lead to lower SO_2 emissions.

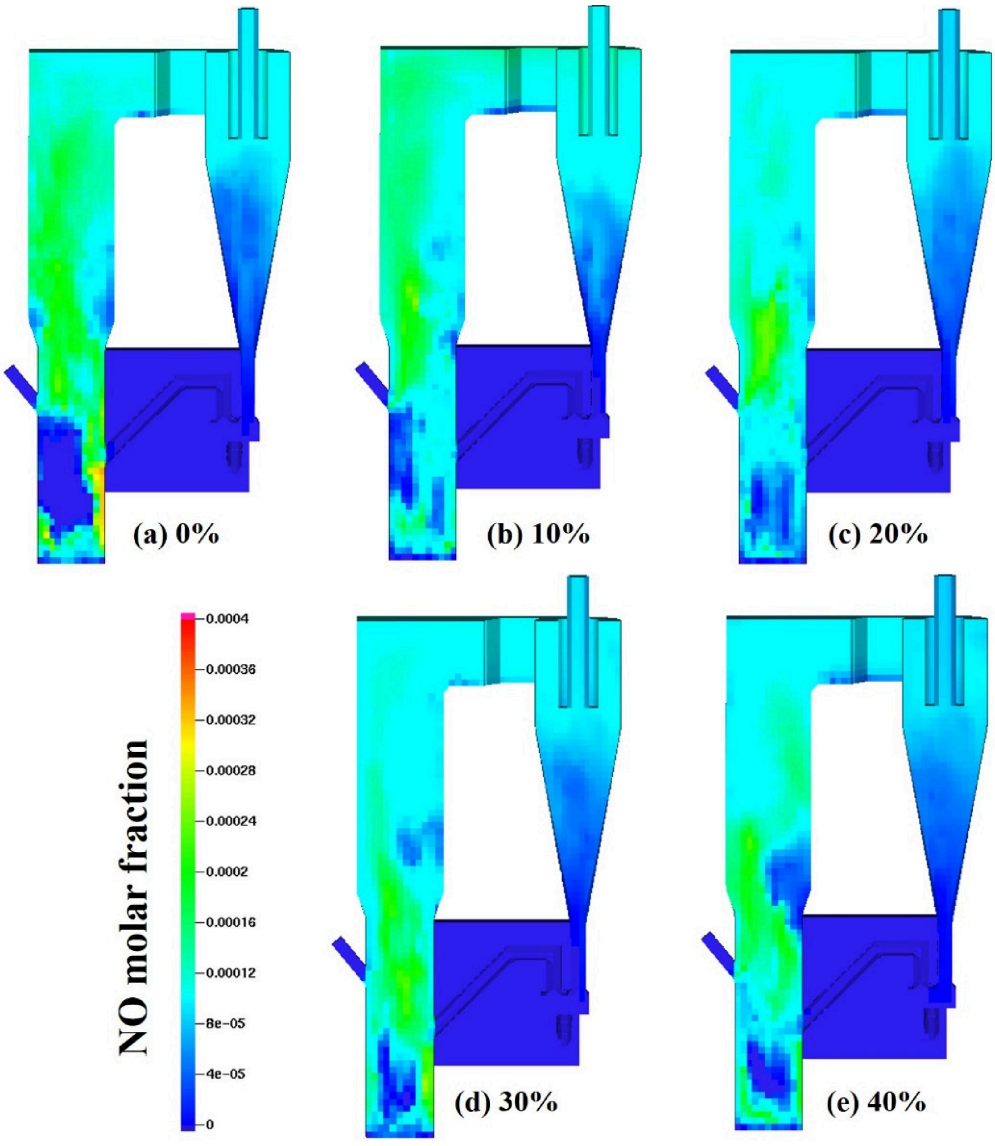


Figure 10. NO molar fraction distribution in circulating fluidized bed boilers at different biomass ratios.

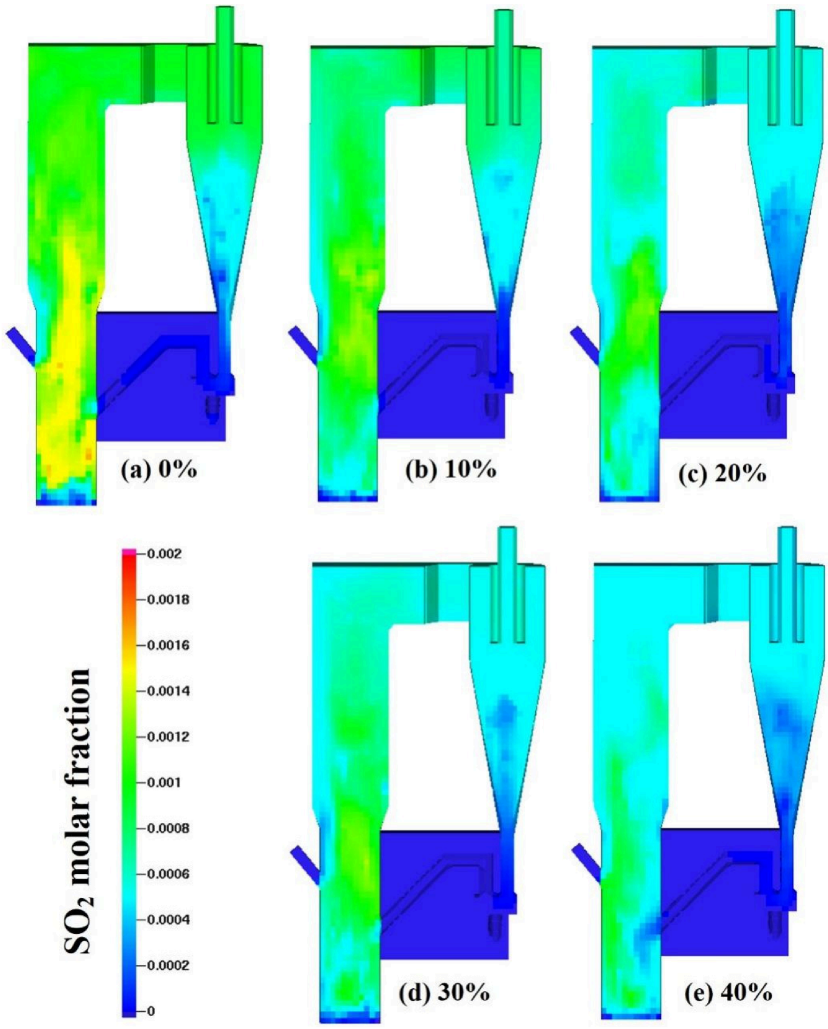


Figure 11. SO_2 molar fraction distribution in circulating fluidized bed boilers at different biomass ratios.

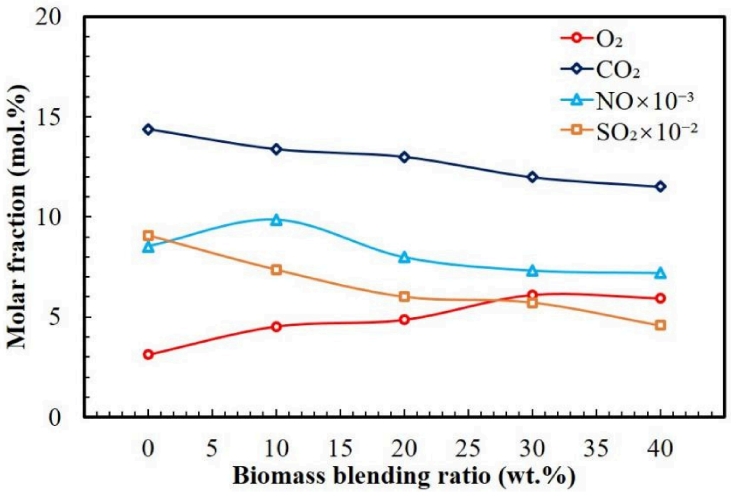


Figure 12. Gaseous molar fractions of cyclone separator outlet at different biomass ratios.

Limitations of the current work should be clarified here. First, only single rice husk biomass is tested; variations in ash composition, volatile fractions and particle sizes of alternative biomass fuels will change bed hydrodynamics and pollutant generation rules, which cannot be fully captured in this study. Second, parametric sensitivity analyses of radiation, drag and heat transfer models are not performed due to the ultra-high com-

putational cost of full-loop industrial MP-PIC simulations. Third, limited measurable industrial data only enables validation of outlet gas components and furnace temperature, while particle velocity and residence time comparisons are absent owing to the opacity and high-temperature environment of the combustion boiler. All above supplementary quantitative analyses will be completed in follow-up small-scale simulation studies with reduced computational consumption.

4. Conclusions

This study successfully developed and validated a comprehensive MP-PIC model for simulating coal-biomass co-combustion in an industrial-scale circulating fluidized bed furnace, integrating experimentally derived pyrolysis kinetics. The addition of rice husk biomass (up to 40 wt.%) does not significantly alter the internal particulate flow hydrodynamics or solid circulation in the circulating fluidized bed, as the system is dominated by the inert bed material. Biomass co-firing reduces the average furnace temperature but leads to a more uniform temperature distribution within the entire furnace at higher blending ratios (30–40 wt.%). Co-firing is highly effective for reducing emissions. A 40 wt.% biomass blend achieved the greatest reductions: 51.99% for net CO_2, 49.50% for SO_2, and 15.70% for NO. The results demonstrate that high-proportion co-firing of rice husk in existing coal-fired circulating fluidized bed is not only feasible but also advantageous for reducing greenhouse gas and pollutant emissions without disrupting stable operation. The MP-PIC methodology proves to be a valuable tool for the design and optimization of co-firing processes. The framework has potential to be extended to various co-firing systems, whereas its applicability for other biomass fuels needs further verification considering the differences in fuel physical and chemical properties.

Supplementary Materials: The following supporting information can be downloaded at https://www.mdpi.com/article/10.3390/pr14132189/s1, Figure S1: The setting of operating conditions for primary air; Figure S2: Particle size distribution for coal; Figure S3: Particle size distribution curve for coal; Figure S4: Particle size distribution for ash; Figure S5: Particle size distribution curve for ash; Figure S6: TG and DTG curves for coal and biomass; Table S1: Particle and parcel statistic information.

Author Contributions: Software, G.J.; Investigation, L.L., J.S. and J.Y.; Writing—original draft, L.L. and G.J.; Writing—review and editing, Y.S.Z.,T.A., D.Z., J.D. and S.C.; Visualization, L.L. and G.J. All authors have read and agreed to the published version of the manuscript.

Funding: This research was financially supported by fund from Key Laboratory of Hubei Province for Coal Conversion and New Carbon Materials (Wuhan University of Science and Technology) (Grant No. WKDM202506).

Data Availability Statement: Data available on request due to restrictions.

Conflicts of Interest: Author Li Liu was employed by the company Anhui Conch Biomass Energy Technol Co., Ltd. The remaining authors declare that the research was conducted in the absence of any commercial or financial relationships that could be construed as a potential conflict of interest.

Nomenclature

A	Area (m^2)
C_D	Drag coefficient (-)
$C_{p,g}$	Specific heat capacity of gas ($J \cdot m^{-3} \cdot K^{-1}$)
$C_{p,s}$	Specific heat capacity of solid ($J \cdot m^{-3} \cdot K^{-1}$)
d_p	Particle size (m)
f_{drag}	Drag force ($N \cdot m^{-3}$)

$\boldsymbol{F}$	Force (N)
F_{wp}	View factor (-)
k_{eff}	Effective thermal conductivity ($W \cdot m^{-1} \cdot K^{-1}$)
k_p	Thermal conductivities of particle materials ($W \cdot m^{-1} \cdot K^{-1}$)
m	Mass (kg)
p	Pressure (Pa)
Pr	Prandtl number (-)
q	Heat flux ($W \cdot m^{-2}$)
Re	Reynolds number (-)
t	Time (s)
T	Temperature (K)
$\boldsymbol{u}_g$	Gas velocity ($m \cdot s^{-1}$)
α	Conversion (-)
α_p	Volume-weighted average of particle emissivity (-)
α_w	Specified emissivity of the wall (-)
α_{wp}	Effective emissivity between wall and particles (-)
β	Interphase momentum exchange coefficient ($kg \cdot m^{-3} \cdot s^{-1}$)
ε_g	Gas volume fraction (-)
ε_s	Particle volume fraction (-)
μ	Viscosity (Pa·s)
ρ_g	Gas density ($kg \cdot m^{-3}$)
σ	Stefan-Boltzmann constant $5.67037442 \times 10^{-8}$ ($kg \cdot s^{-3} \cdot K^{-4}$)
Abbreviation	***Full name***
CFB	Circulating Fluidized Bed
CFD	Computational Fluid Dynamics
CPFD	Computational Particle Fluid Dynamics
CFD-DEM	Computational Fluid Dynamics and Discrete Element Method
DEM	Discrete Element Methods
EHE	External Heat Exchanger
LES	Large Eddy Simulation
MP-PIC	Multiphase Particle-In-Cell
TGA	Thermogravimetric Analysis
TFM	Two-Fluid Model

References

1. Smith, D.S.; Alzina, A.; Bourret, J.; Nait-Ali, B.; Pennec, F.; Tessier-Doyen, N.; Otsu, K.; Matsubara, H.; Elser, P.; Gonzenbach, U.T. Thermal conductivity of porous materials. *J. Mater. Res.* **2013**, *28*, 2260–2272. [CrossRef]
2. Gidaspow, D. Hydrodynamics of fiuidizatlon and heat transfer: Supercomputer modeling. *Appl. Mech. Rev.* **1986**, *39*, 1–23. [CrossRef]
3. Ma, Z.B.; Shan, X.Y.; Cheng, F.Q. Distribution Characteristics of Valuable Elements, Al, Li, and Ga, and Rare Earth Elements in Feed Coal, Fly Ash, and Bottom Ash from a 300 MW Circulating Fluidized Bed Boiler. *Acs Omega* **2019**, *4*, 6854–6863. [CrossRef] [PubMed]
4. Liu, L.; Memon, M.Z.; Xie, Y.; Gao, S.; Guo, Y.; Dong, J.; Gao, Y.; Li, A.; Ji, G. Recent advances of research in coal and biomass co-firing for electricity and heat generation. *Circ. Econ.* **2023**, *2*, 100063. [CrossRef]
5. Fabrizio, S. *Fluidized Bed Technologies for Near-Zero Emission Combustion and Gasification*; Woodhead Publishing: Cambridge, UK, 2013. [CrossRef]
6. Mirek, P. Scaling of Flow Phenomena in Circulating Fluidized Bed Boilers. *Chem. Process Eng. New Front.* **2011**, *32*, 91–100. [CrossRef]
7. Davenport, J. *Statistical-Review-of-World-Energy-2023*; Energy Institute: London, UK, 2023.
8. Cui, Y.; Zou, Y.; Jiang, S.J.; Zhong, W.Q. Combustion Characteristic Prediction of a Supercritical CO2 Circulating Fluidized Bed Boiler Based on Adaptive GWO-SVM. *Acs Omega* **2023**, *8*, 10160–10175. [CrossRef] [PubMed]
9. Zhang, Z.L.; Zeng, Q.D. Numerical simulation and experimental analysis on nitrogen and sulfur oxides emissions during the co-combustion of Longyan anthracite and sawmill sludge. *Fuel* **2019**, *254*, 115611. [CrossRef]

10. Rassai, N.; Boutammachte, N. Environmental impacts analysis of Moroccan olive cake combustion in Stirling motor cogeneration system: Case study. *Heliyon* **2024**, *10*, e28516. [CrossRef] [PubMed]
11. Cundall, P.A.; Strack, O.D.L. Discrete Numerical-Model for Granular Assemblies. *Geotechnique* **1979**, *29*, 47–65. [CrossRef]
12. Adamczyk, W.P. Application of the Numerical Techniques for Modelling Fluidization Process Within Industrial Scale Boilers. *Arch. Comput. Methods Eng.* **2017**, *24*, 669–702. [CrossRef] [PubMed]
13. Yang, S.L.; Wang, S. Shape Effect of the Riser Cross Section on the Full-Loop Hydrodynamics of a Three-Dimensional Circulating Fluidized Bed. *Acs Omega* **2020**, *5*, 5784–5795. [CrossRef] [PubMed]
14. Snider, D.M.; Clark, S.M.; O'Rourke, P.J. Eulerian-Lagrangian method for three-dimensional thermal reacting flow with application to coal gasifiers. *Chem. Eng. Sci.* **2011**, *66*, 1285–1295. [CrossRef]
15. Li, C.L.; Eri, Q. Comparison between two Eulerian-Lagrangian methods: CFD-DEM and MPPIC on the biomass gasification in a fluidized bed. *Biomass Convers. Biorefin.* **2023**, *13*, 3819–3836. [CrossRef]
16. Go, E.S.; Kim, B.S.; Ling, J.L.J.; Oh, S.S.; Park, H.J.; Lee, S.H. In-situ desulfurization using porous Ca-based materials for the oxy-CFB process: A computational study. *Environ. Res.* **2023**, *225*, 115582. [CrossRef] [PubMed]
17. Lu, X.S.; Tan, J.Z.Y.; Maroto-Valer, M.M. Investigation of CO_2 Photoreduction in an Annular Fluidized Bed Photoreactor by MP-PIC Simulation. *Ind. Eng. Chem. Res.* **2022**, *61*, 3123–3136. [CrossRef] [PubMed]
18. Yu, J.H.; Wang, S.; Luo, K.; Li, D.B.; Fan, J.R. Study of biomass gasification in an industrial-scale dual circulating fluidized bed (DCFB) using the Eulerian-Lagrangian method. *Particuology* **2023**, *83*, 156–168. [CrossRef]
19. Guo, M.Y.; Yu, J.H.; Wang, S.; Luo, K.; Fan, J.R. Study of biomass gasification combined with CO2 absorption in a dual fluidized bed (DFB) using the Eulerian-Lagrangian method. *Chem. Eng. J.* **2024**, *483*, 148723. [CrossRef]
20. Henríquez-Vargas, L.; Donoso-García, P.; Lackey, L.; Bravo-Gutiérrez, M.; Cajas, B.; Reyes, A.; Pailahueque, N.; Diaz-Aburto, I.; Bubnovich, V. Modeling of the Solid Stress Tensor in the MP-PIC Method: A Review of Methods and Applications. *Mathematics* **2024**, *12*, 3700. [CrossRef]
21. Dong, T.; Kong, D.L.; Wang, S. Insights into the gas-solid hydrodynamics and thermochemical characteristics in a pilot-scale chemical looping combustion unit using MP-PIC. *Powder Technol.* **2024**, *438*, 119547. [CrossRef]
22. Lin, R.B.; Wang, S.Y.; Tao, Y.J.; Feng, X.J.; Zhang, H.Y. Numerical Simulation and Optimization of Industrial-Scale Fluidized Bed Reactor Coupling Biomass Catalytic Pyrolysis Kinetics. *Energies* **2025**, *18*, 3601. [CrossRef]
23. Zhao, M.; Raheem, A.; Memon, Z.M.; Vuppaladadiyam, A.K.; Ji, G.Z. Iso-conversional kinetics of low-lipid micro-algae gasification by air. *J. Clean. Prod.* **2019**, *207*, 618–629. [CrossRef]
24. Xie, J.; Zhong, W.Q.; Shao, Y.J.; Liu, Q.; Liu, L.H.; Liu, G.Y. Simulation of Combustion of Municipal Solid Waste and Coal in an Industrial-Scale Circulating Fluidized Bed Boiler. *Energy Fuels* **2017**, *31*, 14248–14261. [CrossRef]
25. Mirek, P. Air Distributor Pressure Drop Analysis in a Circulating Fluidized-Bed Boiler for Non-reference Operating Conditions. *Chem. Eng. Technol.* **2020**, *43*, 2233–2246. [CrossRef]
26. Mirek, P.; Klajny, M. Air nozzle design criteria for protection against the backflow of solids in CFB boilers. *Appl. Therm. Eng.* **2018**, *141*, 503–515. [CrossRef]
27. Beetstra, R.; van der Hoef, M.A.; Kuipers, J.A.M. Drag force of intermediate Reynolds number flow past mono- and bidisperse arrays of spheres. *Aiche J.* **2007**, *53*, 489–501. [CrossRef]
28. Babaei, M.; Movahedirad, S. Hydrodynamics of a cold circulating fluidized bed for methanol-to-olefins (MTO) process: Experimental and computational investigation. *Sci. Rep.* **2023**, *13*, 18349. [CrossRef] [PubMed]
29. Shi, X.G.; Sun, R.J.; Lan, X.Y.; Liu, F.; Zhang, Y.H.; Gao, J.S. CPFD simulation of solids residence time and back-mixing in CFB risers. *Powder Technol.* **2015**, *271*, 16–25. [CrossRef]
30. Zhou, W.; Zhao, C.S.; Duan, L.B.; Chen, X.P.; Liang, C. Two-dimensional computational fluid dynamics simulation of nitrogen and sulfur oxides emissions in a circulating fluidized bed combustor. *Chem. Eng. J.* **2011**, *173*, 564–573. [CrossRef]
31. Lian, G.Q.; Zhong, W.Q. Particle-scale investigation of oxy-fuel combustion in a pressurized fluidized bed. *Fuel* **2023**, *342*, 127813. [CrossRef]
32. Cui, Y.; Liu, X.J.; Zhong, W.Q. Simulations of Coal Combustion in a Pressurized Supercritical CO2 Circulating Fluidized Bed. *Energy Fuels* **2020**, *34*, 4977–4992. [CrossRef]
33. Zhong, W.Q.; Xie, J.; Shao, Y.J.; Liu, X.J.; Jin, B.S. Three-dimensional modeling of olive cake combustion in CFB. *Appl. Therm. Eng.* **2015**, *88*, 322–333. [CrossRef]
34. Raheem, D.G.; Yilmaz, B.; Özdogan, S. Comparison of oxygen enriched and oxy-combustion characteristics of lignite in a CFB: Modelling and experimental verification. *Powder Technol.* **2021**, *389*, 355–367. [CrossRef]
35. Shen, X.; Jia, L.; Wang, Y.L.; Guo, B.H.; Fan, H.D.; Qiao, X.L.; Zhang, M.; Jin, Y. Study on Dynamic Characteristics of Residual Char of CFB Boiler Based on CPFD Method. *Energies* **2020**, *13*, 5883. [CrossRef]
36. Desroches-Ducarne, E.; Dolignier, J.C.; Marty, E.; Martin, G.; Delfosse, L. Modelling of gaseous pollutants emissions in circulating fluidized bed combustion of municipal refuse. *Fuel* **1998**, *77*, 1399–1410. [CrossRef]
37. Gungor, A. Two-dimensional biomass combustion modeling of CFB. *Fuel* **2008**, *87*, 1453–1468. [CrossRef]

38. Xie, J.; Zhong, W.Q.; Jin, B.S.; Shao, Y.J.; Liu, H. Three-Dimensional Eulerian-Eulerian Modeling of Gaseous Pollutant Emissions from Circulating Fluidized-Bed Combustors. *Energy Fuels* **2014**, *28*, 5523–5533. [CrossRef]
39. Li, N.; Jiayi, L.; Qigang, D.; Liming, G.; Dayong, X.; Zhongzhi, Y.; Xiaofeng, L. Study on the Uniformity of Secondary Air of a 660 MW Ultra-Supercritical CFB Boiler. *Energies* **2022**, *15*, 3604. [CrossRef]
40. Mirek, P. Field Test of Superheater Pipes Vibration Caused by Sound Energy in the 235 MWe Circulating Fluidized Bed Boiler. *Energies* **2021**, *14*, 7678. [CrossRef]
41. Liu, Z.; Li, W.H.; Zhang, Y.S.; Wang, J.W.; Orndorff, W.; Pan, W.P. Influence of biomass on coal combustion based on thermogravimetry and Fourier transform infrared spectroscopy. *J. Therm. Anal. Calorim.* **2015**, *122*, 1289–1298. [CrossRef]
42. Moreno, J.; Schmid, M.; Scharr, S.; Scheffknecht, G. Oxy-Combustion of Solid Recovered Fuel in a Semi-Industrial CFB Reactor: On the Implications of Gas Atmosphere and Combustion Temperature. *Acs Omega* **2022**, *7*, 8950–8959. [CrossRef] [PubMed]
43. Rohr, A.C.; Campleman, S.L.; Long, C.M.; Peterson, M.K.; Weatherstone, S.; Quick, W.; Lewis, A. Potential Occupational Exposures and Health Risks Associated with Biomass-Based Power Generation. *Int. J. Environ. Res. Public Health* **2015**, *12*, 8542–8605. [CrossRef] [PubMed]

Disclaimer/Publisher's Note: The statements, opinions and data contained in all publications are solely those of the individual author(s) and contributor(s) and not of MDPI and/or the editor(s). MDPI and/or the editor(s) disclaim responsibility for any injury to people or property resulting from any ideas, methods, instructions or products referred to in the content.